Title

Development of a preclinical CCD-based temperature modulated fluorescence tomography platform.

Journal

Biomedical Optics Express, 13(11)

ISSN

2156-7085

Authors

Nouizi, Farouk
Erkol, Hakan
Nikkhah, Deniz
et al.

Publication Date

2022-11-01

DOI

10.1364/boe.470723

Peer reviewed

Research Article | Vol. 13, No. 11 / 1 Nov 2022 / Biomedical Optics Express 5740
Biomedical Optics EXPRESS

Development of a preclinical CCD-based temperature modulated fluorescence tomography platform

FAROUK NOUIZI,[1,2,*] HAKAN ERKOL,[3] DENIZ NIKKHAH,[1] TIFFANY C. KWONG,[1] AND GULTEKIN GULSEN[1,2]

[1]Tu and Yuen Center for Functional Onco-Imaging, Department of Radiological Sciences, University of California Irvine, CA 92697, USA
[2]Chao Family Comprehensive Cancer Center, University of California Irvine, CA 92697, USA
[3]Department of Physics, Bogazici University, Bebek, 34342, Istanbul, Turkey
[*]fnouizi@uci.edu

Abstract: In preclinical research, fluorescence molecular tomography (FMT) is the most sensitive imaging modality to interrogate whole-body and provide 3D distribution of fluorescent contract agents. Despite its superior sensitivity, its mediocre spatial-resolution has been the main barrier to its clinical translation. This limitation is mainly due to the high scattering of optical photons in biological tissue together with the limited boundary measurements that lead to an undetermined and ill-posed inverse problem. To overcome the limitations of FMT, we previously introduced a novel method termed, Temperature Modulated Fluorescence Tomography (TMFT). TMFT utilizes thermos-sensitive fluorescent agents (ThermoDots) as a key component and localizes them with high-intensity focused ultrasound (HIFU). Scanning the focused HIFU beam having a diameter Ø = 1.3 mm across the tissue while monitoring the variation in the measured fluorescence signals reveals the position of the ThermoDots with high spatial accuracy. We have formerly built a prototype TMFT system that uses optical fibers for detection. In this paper, we present an upgraded version using a CCD camera-based detection that enables non-contact imaging. In this version, the animal under investigation is placed on an ultrasound transparent membrane, which eliminates the need for its immersion in optical matching fluids that were required by the fiber-based system. This CCD-based system will pave the way for convenient and wide-spread use of TMFT in preclinical research. Its performance validation on phantom studies demonstrates that high spatial-resolution (~1.3 mm) and quantitative accuracy in recovered fluorophore concentration (<3% error) can be achieved.

1. Introduction

Fluorescence diffuse optical tomography (FMT) reveals the distribution and concentration of fluorophores in bio-tissue, using non-ionizing radiation and low-cost instrumentation, which make it ideal for *in vivo* imaging [1,2]. The high scattering of optical photons in biological tissue is one of the major obstacles that prevents FMT from playing a significant role in clinical settings [3]. Together with the limited boundary measurements makes the FMT image reconstruction process undetermined and ill-posed, which challenges the performance of FMT in deep tissue [3,4]. It has been shown that structural information obtained from other anatomical imaging modalities such as X-ray CT, Magnetic Resonance Imaging (MRI), or ultrasound can be used as *a priori* information to guide and constrain the FMT image reconstruction algorithm, and hence improves its spatial-resolution and quantitative accuracy [5–11]. However, besides using ionizing radiations or expensive instrumentations, the main disadvantages of this approach is that anatomical contrasts do not always correlate with molecular ones [12]. The boundary of the delineated diseased tissue by anatomic imaging modalities may often misguide the FMT

#470723 https://doi.org/10.1364/BOE.470723
Journal © 2022 Received 18 Jul 2022; revised 25 Sep 2022; accepted 26 Sep 2022; published 12 Oct 2022

Biomedical Optics EXPRESS

image reconstruction algorithm. Therefore, a different approach, where the second modality interacts with FMT and modulates its signals with high resolution working in harmony would be the preferable solution to obtain better FMT spatial- resolution.

Nearly a decade ago, we introduced a new imaging modality called "Temperature Modulated Fluorescence Tomography (TMFT)", that can efficiently undertake this challenging task [13]. Utilizing temperature sensitive fluorescent contrast agents and highly localized heating power of high intensity focused ultrasound (HIFU), TMFT could provide 3D fluorescence images in tomographic mode. Mainly TMFT was geared towards increasing the spatial-resolution and quantitative accuracy of conventional FMT. Several other groups also have spent extensive efforts to improve the performance of the fluorescence imaging utilizing different temperature sensitive fluorescent contrast agents but in planar imaging mode [14–16].

TMFT is based on two main components: temperature sensitive fluorescence agent (ThermoDots), and HIFU [17–24]. The activatable property of the ThermoDots depends on two main ingredients: Indocyanine-Green (ICG) and pluronic polymers [25,26]. The key advantage of ThermoDots is that their fluorescence signal intensity and life-time are temperature dependent [27–30]. The principle of TMFT is a novel way of synergic integration of two modalities (HIFU and FMT) instead of the conventional way of using them sequentially one after the other. In TMFT, ultrasound is no longer used to obtain usual structural *a priori* information, but instead to provide localized heating by focusing acoustic waves in a focal zone (Ø = 1.3 mm), which in turn helps TMFT localizing the ThermoDots within the tissue. Briefly, conventional FMT is first performed by acquiring CCD images of the fluorescence emission from the top of the volume under investigation, while a point-source excitation beam is scanned from its bottom on a predetermined grid. The conventional FMT image is then reconstructed and segmented to define regions of interests (ROI). Following that the HIFU and excitation light beam are scanned together on a smaller but denser grid defined over the defined ROI selected on the conventional FMT images. In step and shoot mode, the fluorescence emission at each grid position is acquired with and without activating the HIFU beam. The absence of ThermoDots is verified by the lack of fluorescence signal increase [21]. However, a sudden increase in the signal is observed if the HIFU and excitation light beam coincide with presence of ThermoDots. This variation in the fluorescence emission signal detected by the CCD is used to construct a binary mask over this ROI. Finally, this binary mask having a much higher resolution (Ø = 1.3 mm) compared to conventional FMT is used to guide and constrain the conventional FMT reconstruction algorithm. Basically, this binary mask is a more versatile *functional a priori* that directly maps the fluorophore distribution, unlike the conventional *structural a priori* derived by anatomic imaging modalities [17–23]. Hence, TMFT can provide much higher quantitative accuracy and superior spatial-resolution compared to FMT alone or when conventionally combined with an anatomical imaging technique.

In this paper, we present the new CCD-based TMFT small animal imaging system. The old fiber-based TMFT prototype used optical fibers to detect the fluorescence signals at the tissue boundary [20–24]. As for any fiber-based optical tomography system, the imaging results highly depend on the quality of calibration of all detectors with respect to one another. Most importantly, stand-alone fiber-based optical tomography systems generally necessitates the immersion of the animal into optically matching liquids [31,32]. The main reason for this is that source and detector fibers are generally fixed in a certain regular geometry (*i.e.* rectangular or circular) around the imaging volume to avoid the need for their localization every imaging session. Hence, the empty space between the animal boundary and the optical fibers is filled with an optical matching fluid.

The new CCD-based TMFT system enables free-space detection since the camera is placed on top of the animal while the HIFU transducer as well as the excitation light collimator are scanned directly under the animal [33,34]. A computer-controlled translation stage is used to

Biomedical Optics EXPRESS

move them in tandem on a predefined grid while CCD images are acquired at each point with and without activating the HIFU beam. This new CCD-based set-up allows us to place the subject under investigation over an ultrasound-transparent membrane eliminating the need for immersion in matching fluids. Hence, the new prototype is very user friendly and convenient for preclinical imaging, where high throughput is critical. Placing the animals in their natural prone position is also important to keep internal organs from displacing. Therefore, we believe that this CCD-based approach will drastically increase the potential of TMFT and its wide-spread in preclinical research.

2. Materials and methods

2.1. Temperature sensitive contrast agents (ThermoDots)

ThermoDots are thermo-sensitive fluorescent nanoprobes composed of a thermo-sensitive micelle made from Pluronic polymers that encapsulates indocyanine green (ICG) [28]. Changing the ThermoDots environment temperature, changes the hydrophobicity and hydrophilicity of the core and cornea of the micelle, which induces a change in the solvent polarity. This results in a change in the quantum efficiency of the loaded ICG micelles. Consequently, ThermoDots emit a fluorescence signal similar to a solution of ICG alone, at low temperature. This emitted signal increases several folds when the temperature of ThermoDots is raised [25,26,29]. Several TMFT phantom validation studies have been conducted [23,24] with ThermoDots synthesized using polymer F127, Fig. 1. These ThermoDots have a thermal dynamic range design around the average room temperature (17-23 °C).

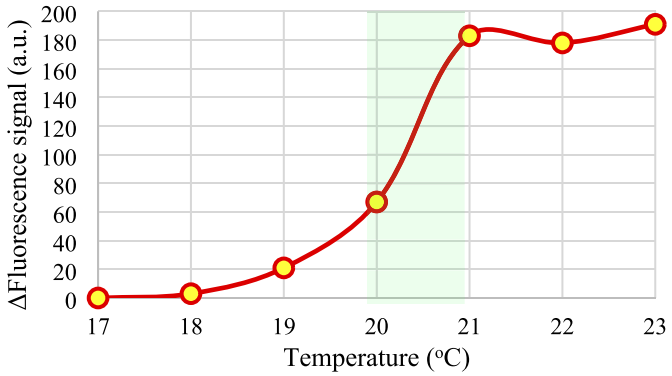

Fig. 1. The temperature dependent fluorescence emission of the ThermoDots designed for the phantom study in the range of 17-23 °C. The highlighted area shows the range used for the experiments performed in this paper.

The temperature range of the ThermoDots can be adjusted by varying the type of the polymer and/or the concentration of the used ICG [35]. For *in vivo* studies, other versions of our ThermoDots have been synthesized within the framework of our collaboration with our industrial collaborators, InnoSense LLC (Torrance, CA) [28]. These other versions are responsive in higher temperature ranges, which are more adequate for *in vivo* studies. Currently, we are working on conjugating our ThermoDots with antibodies to synthesize specific disease targeting to improve their performance for *in vivo* studies.

2.2. Instrumentation:

We upgraded our fiber-based TMFT system to a CCD-based one, Fig. 2. The old fluorescence signal detection unit consisting of fiber bundles is replaced with a CCD camera (ColdBlueTM,

Biomedical Optics EXPRESS

PerkinElmerTM optoelectronics, USA). In this configuration, the camera is placed on top of the animal to enable free-scape detection, which in turn eliminates the demanding task of immersing the animals in matching fluid, making the new system user friendly. Here, the animal is placed on a HIFU transparent membrane, that supports the animal and keeps it in contact with the water used as an acoustic medium for the HIFU. The HIFU transducer (H102, Sonic Concepts, Inc., Bothell, WA) has a focal length of ~62 mm and produces a cylindrical focal zone of ~1.3 mm in diameter and 10 mm in height. A signal generator (33220A, Agilent Technologies) is used to drive the transducer in continuous-wave mode with an operating frequency of 1.025 MHz. The output signal is amplified using a 100-Watt amplifier (155LCRH, Kalmus, USA). A variable attenuator (355C, Agilent Technologies) is used at the input of the amplifier to adjust the power and use the HIFU in low power mode. The HIFU is placed in the water tank underneath the membrane to perform the scanning from the bottom of the animal, Fig. 2(a). Also, the excitation light source collimator is attached to the center of the HIFU making both beams aligned and concentric. This acquisition scheme allows us to achieve a uniform detection sensitivity throughout the whole animal. Since recovering accurate FMT images *in vivo* requires the prior knowledge of the optical properties of the whole animal, diffuse optical tomography (DOT) is performed at the fluorescence excitation and emission wavelengths of the ThermoDots. Therefore, a computer-controlled filter wheel is used to easily switch between DOT and FMT measurements, which respectively requires no filter and fluorescence band-pass filters.

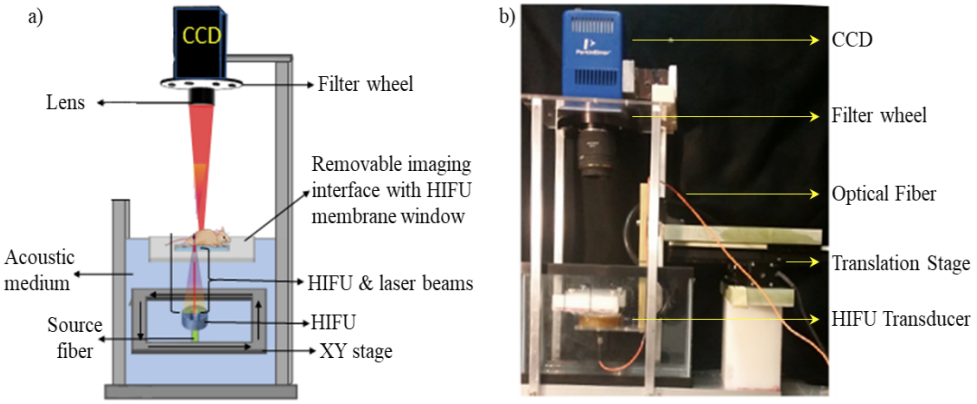

Fig. 2. Schematic (a) and picture (b) of the CCD-Based TMFT system.

Figure 2(b) shows a picture of our current camera-based *in vivo* small animal dedicated TMFT system. A 785 nm laser is used to excite the ThermoDots. The laser and its driver are placed in a separate box located next to the system. The output of the laser is transferred to the TMFT system using an optical fiber. A computer-controlled translation stage is used to move them in tandem on a predefined grid while CCD images are acquired at each point with and without activating the HIFU beam.

2.3. Data acquisition

2.3.1. Conventional FMT data acquisition

The subject under investigation is placed on a thin membrane that is transparent for both optical ultrasound waves. A 785 nm excitation laser beam is scanned from the bottom of membrane over a 5×5 grid using the translational stage, while CCD images are acquired from the top. The camera allows to acquire up to 2280 pixels x 1528 pixels images. In this work, a factor of 4 is used to bin the pixels during acquisition to increase signal strength, resulting in 570 pixels x

Biomedical Optics EXPRESS

382 pixels images with a pixel size of 0.25 mm × 0.25 mm. Each image is acquired using an integration time of two seconds. An 830 ± 10 nm bandpass filter is placed in front of the camera to eliminate the excitation light and only detect the fluorescence emission of the ThermoDots. A total of 25 images are acquired corresponding to this 5 × 5 grid. At every grid position (5 mm apart), the excitation light is turned on and a fluorescence image is acquired. Including the positioning time, the total imaging time is around one minute for the conventional FMT. To improve the accuracy of the FMT, it is also important to acquire DOT data, which provides the optical absorption map. DOT data is sequentially acquired on the same grid using a 785 nm then a 830 nm laser but without use of the bandpass fluorescence filter. These extra DOT scans are also completed under a minute. The absorption maps reconstructed by the DOT inverse solver at the excitation and emission wavelengths of the ThermoDots are later used in the FMT inverse solver to increase its accuracy [36].

2.3.2. HIFU Scan and functional a priori

Once the FMT data acquisition and image reconstruction steps are completed, an ROI is selected on the conventional FMT images by applying a threshold at full-width-half-maximum (FWHM). This ROI determines the area over which the HIFU scan is performed. Figure 3 shows an example for a phantom containing a 3-mm-diameter inclusion filled with ThermoDots. The cross-sectional image of the true ThermoDots distribution is given at Fig. 3(a). The reconstructed distribution of ThermoDots using the conventional FMT for the same area is given in Fig. 3(b). As seen from the figure, the conventional FMT does not have enough resolution to recover the 3 mm inclusion. The ROI selected at FWHM is shown with a green solid-line contour. Once the ROI is selected, a much denser grid with 0.65mm steps (*i.e.* half of the HIFU beam size ~1.3 mm) is placed on the ROI and HIFU scan is performed.

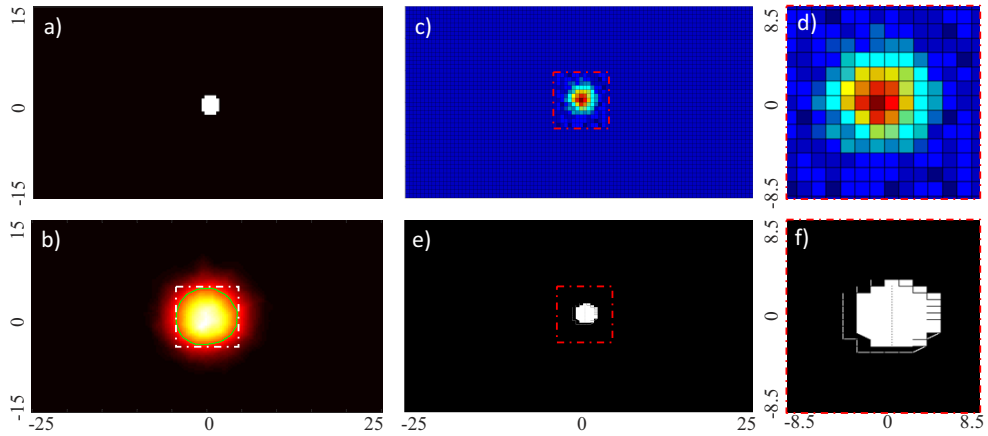

Fig. 3. Steps of the TMFT functional a priori mask recovery presented using an example medium containing a 3-mm-dimeter inclusion at the center filled with ThermoDots. a) Binary map showing the real position of the inclusion. b) conventional FMT. An ROI is delignated over the FMT image by segmenting it at FWHM (Green solid-line contour). A rectangular ROI is defined around the FMT segmented ROI as represented with the white dashed-line square. c) fluorescence signal variation map obtained by scanning the HIFU over the rectangular ROI using a step-and-shoot mode d) closer look of the signal variation map. e) Binary map generated by segmenting the fluorescence variation map. f) closer look shows the shape of the recovered inclusion.

The HIFU transducer creates a zone of intense heat at its focal zone by focusing the acoustic waves. This localized heating (<2 °C) allows heating the targeted area with minor effect to

Biomedical Optics EXPRESS

surrounding tissues. TMFT utilizes the focused ultrasound at low power mode yielding a slight heating for only two seconds, which is set by the integration time of the CCD camera . During the TMFT HIFU scanning, the excitation light and focused ultrasound beam are scanned over this dense grid while the fluorescence emission data is acquired with the CCD camera, first without and later with a brief HIFU pulse. For this particular example, 81 data points over a 9×9 grid is utilized that brings the total HIFU scan time to ~5 min. When the ThermoDots are hit by the HIFU beam, the signal increases, which verifies their presence [13,21]. This variation in the fluorescence emission signal detected by the CCD is used to construct a binary mask over this dense grid, Fig. 3(c). A closer look of this binary mask is given in Fig. 3(c). Since this binary mask has much higher resolution compared to the ROI determined by low resolution FMT, it can be used as a more versatile *functional a priori* that directly maps the fluorophore distribution, unlike the conventional *structural a priori* derived by anatomic imaging modalities [13,17–23,27]. Utilizing *soft a priori* approach, TMFT can provide much higher quantitative accuracy and superior spatial-resolution compared to FMT alone or when conventionally combined with an anatomical imaging technique.

2.4. TMFT image reconstruction algorithm

Like conventional FMT, the mathematical framework for TMFT consists in modeling the excitation light propagation, its absorption by the fluorophore and conversion to emission light, then the propagation of the later within the imaged medium using the coupled diffusion equation [37–41]. Nevertheless, since the advantage of TMFT is employing temperature sensitive fluorophores, a thermally dependent quantum yield of fluorescence, $\eta(T)$, is added to the right-hand-side of the second equation. Thus, the modified forward problem of TMFT allows calculating the density of emission photons, Φ_m^T, emitted from the ThermoDots at temperature T [13,21]:

$$\begin{cases} \nabla[D_x \nabla \Phi_x(r)] - (\mu_{ax} + \mu_{af})\Phi_x(r) = -q_0(r) \\ \nabla[D_m \nabla \Phi_m^T(r)] - \mu_{am}\Phi_m^T(r) = -\Phi_x(r)\eta(T)\mu_{af} \end{cases} \tag{1}$$

where $\mu_{af} = 2.303.\varepsilon.C$ is the absorption coefficient of fluorescence, with ε and C being respectively the molecular extinction coefficient and the concentration of the fluorophore. $\Phi_x(r)$ is the excitation photon density. The diffusion coefficient is defined by $D = \frac{1}{3(\mu_a + \mu_s')}$, with μ_a and μ_s' being respectively the absorption and reduced scattering coefficients of the medium [21,32]. The subscripts x and m represent the excitation and the emission wavelengths, respectively.

The TMFT images are reconstructed by solving the inverse problem that aims to minimize the difference between the fluorescence fluence measured at the surface of the medium and the one calculated by solving Eq.1:

$$\Omega(\mu_{af}) = \sum_{i=1}^{N_s} \sum_{j=1}^{N_d} (\Im_{ij}^T - F_{ij}^T(\mu_{af}))^2 \tag{2}$$

where $\Im_{ij}^T$ is the set of emission light fluence measured at temperature T. $F_{ij}^T(\mu_{af})$ is the set of simulated emission light fluence, which is calculated by solving the forward problem defined by Eq.1. N_s and N_d respectively represent the total number of sources and detectors. The cost function in Eq.2 is minimized using the Levenberg-Marquardt method while iteratively updating the vector of unknowns μ_{af} by [24,39,42–45]:

$$X_{n+1} = X_n + (J^T J + \lambda I)^{-1} J^T (\Im - F) \tag{3}$$

where X represents the unknown vector of μ_{af}, J is the Jacobian matrix. Unfortunately, the reconstructed μ_{af} map at the end of this process is not quantitatively accurate and cannot recover

Biomedical Optics EXPRESS

the fluorescence targets with high spatial-resolution. In order to incorporate the TMFT soft *a priori* information, a penalty matrix describing the binary mask retrieved using the HIFU scan is implemented [37]. The penalty matrix L can be obtained as follow [21,46]:

$$L_{ij} = \begin{cases} 0 & \text{i and j not in the same region} \\ -\frac{1}{N_r} & \text{i and j in the same region, i} \neq \text{j} \\ 1 & i = j \end{cases} \tag{4}$$

where N_r represents the number of nodes included in each region r. The penalty matrix, L, is then implemented into the FMT inverse problem, which is solved a second time utilizing the *a priori* information that helps guide and constrain the conversion of the image reconstruction algorithm. Once again, the inverse problem is solved iteratively by updating the unknown μ_{af} using the Levenberg-Marquardt method:

$$X_{n+1} = X_n + (J^T J + \lambda L^T L)^{-1} J^T (\Im - F) \tag{5}$$

Solving the inverse problem as defined by Eq. (5) significantly improves the quality of the fluorescence images allowing to achieve a much superior quantitative accuracy.

3. Results

To test the performance of our CCD-based TMFT system, we investigate its ability to accurately recover the size, shape, position, and concentration of inclusions filled with ThermoDots and embedded inside tissue-like agarose phantoms. Two rectangular $50 \times 30 \times 17\ \text{mm}^3$ agarose gel phantoms are utilized, Fig. 4(a) and Fig. 5(a). Intralipid (0.5%) and Indian ink are added to the agarose gel to set the absorption and reduced scattering coefficients of the phantoms to be $0.01\ \text{mm}^{-1}$ and $0.8\ \text{mm}^{-1}$, respectively [47]. The origin of the spatial coordinates is set to be at the bottom center of the phantoms. To create a region with ThermoDots accumulation within the phantoms, a 3-mm-diamter and 10-mm-height cylindrical glass tube is first inserted at the center of the first phantom along its z-axis. The top side of the tube is located 4 mm below the upper surface of the phantom, Fig. 4(a). The second phantom is made by inserting two similar tubes at y = 3 mm and at y = -3 mm, Fig. 5(a). These tubes are used to mimic the accumulation of ThermoDots at a tumor within the animal body.

The fluorescence absorption maps that are directly related to the ThermoDots distribution recovered with conventional FMT, and TMFT are compared to the actual values. First, to recover the absorption and reduced scattering coefficients of the phantom, a set of DOT data is acquired while no filter is placed in front of the camera lens [48]. As the absorption and reduced scattering coefficients of the phantom at the excitation and emission wavelengths are nearly equal (~1% difference), the DOT data is only acquired at the excitation wavelength, 785 nm. The averaged recovered optical properties of the phantoms' background are $\mu_a = 0.011\ \text{mm}^{-1}$ and $\mu_s' = 0.81\ \text{mm}^{-1}$. Next, conventional FMT measurements are acquired, and the recovered DOT optical properties are used as optical *functional a priori* information in the conventional FMT reconstruction process, Eq.3. Then, the HIFU is scanned to create the binary mask describing the location, size, and shape of the embedded tubes with high spatial-resolution. Finally, the obtained binary map is implemented as a soft *a priori* within the TMFT reconstruction algorithm to recover the concentration of the ThermoDots using Eq. (4) [23,46].

3.1. Single inclusion phantom

Figure 4 shows the results obtained using the first phantom bearing the single 3-mm-diameter inclusion. To solve the forward problem, the geometry of the phantom is built using the CAD

Biomedical Optics EXPRESS

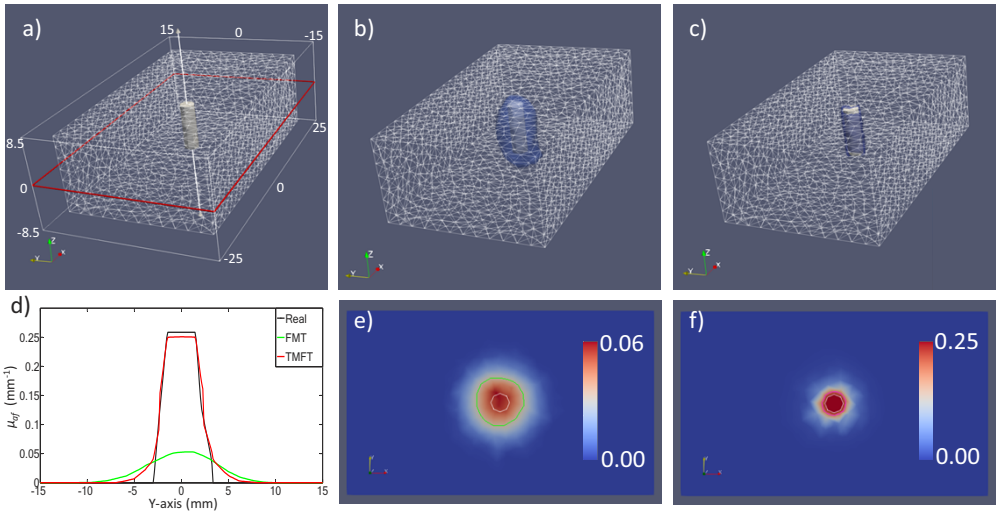

Fig. 4. a) 3D geometry and mesh of the phantom bearing a single 3-mm-diamter inclusion at its center. The tube is shown as a white surface isosurface. The red rectangular boxes show the slices at which figures (e-f) are presented. Reconstructed 3D fluorescence absorption images segmented at full width at half maximum: b) conventional FMT, and c) TMFT. d) The profiles of the fluorescence absorption along the Y-axis: Real (black), recovered using conventional FMT (green), and TMFT (red). Cross-section of the fluorescence absorption reconstructed using e) conventional FMT, and f) TMFT, at z=0 mm. The real contour is shown in white, while the contour of the recovered fluorescence absorption is shown in green (e) and red (f).

toolbox of COMSOL Multiphysics [49], Fig. 4(a). The COMSOL meshing toolbox is then used to generate two meshes, a homogenous and a heterogenous one to be respectively used for conventional FMT and TMFT. First, the homogenous mesh is generated using a maximum element size set to 0.25 mm and by considering only the outer geometry of the phantom. The homogenous mesh consists of 24929 tetrahedral elements connected at 4940 nodes. Second, the heterogenous mesh is generated with the same maximum element size, but by also considering the inclusion boundaries retrieved from the TMFT HIFU-derived mask. The heterogenous mesh consists of 25102 tetrahedral elements connected at 4965 nodes.

The reconstructed fluorescence absorption maps of the ThermoDots (μ_{af}) using conventional FMT and TMFT are shown in Fig. 4(b,e) and Fig. 4(c,f), respectively. Although FMT successfully localizes the inclusion position, it recovers a large fluorescent blob around it. Consequently, the fluorescence absorption is drastically underestimated at 0.053 ± 0.030 mm^{-1}, which represents an error of ~80%. This is mainly due to the fact that the recovered fluorescence is attributed to an area that is larger than the real 3-mm-diamter cylindrical tube volume. The standard deviation is calculated by repeating each of the image reconstruction five times using different regularization parameter and initial fluorophore values.

On the other hand, the TMFT HIFU-derived binary mask localizes the inclusion with high accuracy prior to any reconstruction process. To recover the concentration of ThermoDots within the tube, this binary mask is used as soft *a priori* to solve the FMT inverse problem [20,21,23,24]. The resultant TMFT fluorescence absorption map illustrates the superior spatial-resolution and quantitative accuracy compared to conventional FMT, Fig. 4(c,f). TMFT not only recovers the true size, shape, and position of the true fluorescent inclusion, but also recovers the fluorescence absorption with high accuracy at 0.255 ± 0.008 mm^{-1}, which represents an error less than 2%.

Biomedical Optics EXPRESS

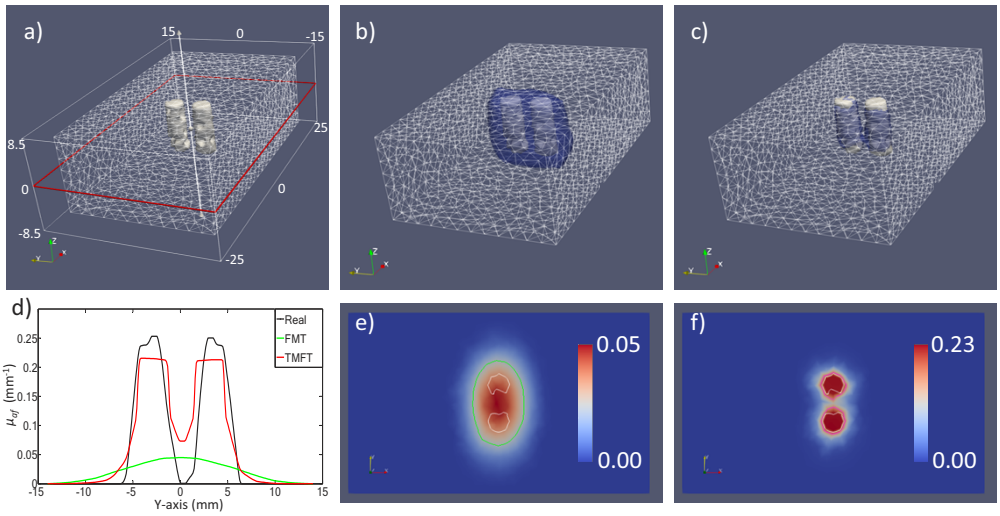

Fig. 5. a) 3D geometry and mesh of the phantom bearing two 3-mm-diamter tubes. The tubes are shown as a white surface isosurface. The red rectangular boxes show the slices at which figures (e-f) are presented. Reconstructed 3D fluorescence absorption images segmented at full width at half maximum: b) conventional FMT, and c) TMFT. d) The profiles of the fluorescence absorption along the Y-axis: Real (black), recovered using conventional FMT (green), and TMFT (red). Cross-section of the fluorescence absorption reconstructed using e) conventional FMT, and f) TMFT, at z=0 mm. The real contour is shown in white. The non-circular shape of the tube is due to the interpolation to the mesh nodes. The contour of the recovered fluorescence absorption is shown in green (e) and red (f).

Indeed, TMFT relies on the acoustics waves from the focused ultrasound transducer and is therefore not constrained by the same scattering and absorption limitations as optical waves. Consequently, TMFT is more accurate at recovering the correct size, shape and position of the ThermoDots, Fig. 4(c,f). Unlike conventional FMT, the TMFT fluorescence distribution is mainly confined within the real boundaries of ThermoDots tube. The irregularities in the recovered inclusion contour are only a result of the shape of the mesh tetrahedral elements.

To better observe the TMFT improvement to the quality of the reconstructed FMT images, profiles are carried-out along the Y-axis, as can be seen on Fig. 4(d). In comparison, conventional FMT greatly overestimated the diameter of the tube and recovered a large blob with an average diameter of size 7.4 mm. On the other hand, TMFT nearly recovered the exact diameter of the tube, with a slight overestimation of only 0.5 mm. We previously demonstrated that this slight error is the result of the interpolation from the mesh to the Cartesian grid image [23]. Indeed, this error is never greater than the size of a single tetrahedral element from each side of the inclusion.

3.2. Double inclusion phantom

The TMFT results obtained using the second phantom bearing the two 3-mm-diameter inclusions are shown in Fig. 5. Like the single phantom study, the geometry of the phantom is built using the CAD toolbox of COMSOL Multiphysics, Fig. 5(a). The COMSOL meshing toolbox is then used to generate two meshes, a homogenous and a heterogenous one to be respectively used for conventional FMT and TMFT. First, the homogenous mesh is generated using a maximum element size set to 0.25 mm and by considering only the outer geometry of the phantom. The homogenous mesh consists of 22154 tetrahedral elements connected at 4430 nodes. Second, the

Biomedical Optics EXPRESS

heterogenous mesh is generated with the same maximum element size, but by also considering the inclusion boundaries retrieved from the TMFT HIFU-derived mask. The heterogenous mesh consists of 25217 tetrahedral elements connected at 4990 nodes. The reconstructed fluorescence absorption map of the ThermoDots (μ_{af}) using conventional FMT is presented in Fig. 5(b,e). As expected, FMT is not able to resolve the two inclusions due to the relatively small 3 mm distance between them. Instead, it recovers a large blob that surrounds both tubes together. Consequently, the fluorescence absorption is drastically underestimated at 0.046 ± 0.070 mm^{-1}, which represents an error of ~84%. However, TMFT is able to resolve the two inclusions, as can be observed in Fig. 5(c,f).

The high quality of these fluorescence absorption maps demonstrates the superiority of TMFT over conventional FMT in terms of spatial-resolution and quantitative accuracy. TMFT not only resolves the two tubes but also recovers a highly accurate estimation of their true size, shape, and position. Thus, the fluorescence absorption is reconstructed with high accuracy at 0.223 ± 0.014 mm^{-1}.

The TMFT improvement to the quality of the fluorescence images is better seen on the profiles carried-out along the Y-axis, as can be seen on Fig. 5(d). The profiles of the blob recovered using conventional FMT show that the tubes are not resolved. Instead, a large blob of diameter 14.6 mm in the Y-direction is recovered. As can be observed, the blob is only elongated in the Y-direction due to the position of the two tubes. In fact, no additional elongation is observed in the X-direction with a recovered diameter of 7.6 mm, which is in agreement with the results obtained using the single inclusion phantom. Here again, TMFT nearly recovered the exact diameter of the tubes, with a slight overestimation of only 0.3 mm. It is worth noting that the quality of the reconstruction is better than the presented profiles, which show a shift of the upper tube by 0.6 mm to the center of the phantom. This shift is unfortunately emphasized due to the interpolation of the recovered μ_{af} to generate the profiles. In fact, the center of gravity of both the real and TMFT recovered upper tube are perfectly aligned with a slight shift less than 0.1 mm, which is insignificant considering the diffuse optics spatial-resolution.

4. Discussion and conclusion

Compared with other optical molecular imaging methods, FMT has the characteristics of high sensitivity, low cost, safety and reliability. Hence, it has become the main optical molecular imaging technology for preclinical research. Although most of the studies are utilizing 2D planar fluorescence imaging, more realistic animal models such as orthotopic and transgenic models necessitate 3D tomographic imaging. However, the resolution of the FMT is the main barrier for its wide-spread use. An intriguing way of improving the FMT resolution is utilization of temperature sensitive contrast agents together with the highly localized heating capability of HIFU. Nevertheless, the dedicated instrumentation should be a convenient high throughput one for successful implementation in preclinical research setting.

Our previous fiber-based TMFT system unfortunately necessitated immersing the animal into optical matching fluids. In this current design, we alleviated this problem by using a CCD camera and placing the subject under investigation on an ultrasound and light transparent membrane. Also, upgrading the TMFT instrumentation from a fiber-based to a camera-based system offered several technical advantages. One of which is the elimination of the fluorescence data calibration, which was necessary due to the difference in performance between the multiple acquisition channels used in the fiber-based system. Similarly, the laser source power calibration between the six laser sources used in the fiber-based version of TMFT is omitted in this new system design that utilizes a single laser source. More importantly, the new acquisition scheme allows us to achieve a uniform detection sensitivity throughout the whole animal body. This is achieved thanks to constant alignment and moving of the laser source point with the HIFU hot spot. In fact, this allows to obtain the same density of excitation photons at each HIFU scanning position,

Biomedical Optics EXPRESS

which results in a uniform sensitivity throughout the whole animal body. This feature was not possible with the fiber-based system. In addition, since the construction of the TMFT mask is mainly based on the difference between fluorescence signals acquired with and without HIFU irradiation, having sufficiently high photon density at the HIFU hot spot is highly advantageous.

We have demonstrated its feasibility with phantoms mimicking animal tissue. The CCD-based system provided the same performance in FMT as the fiber-based system. The TMFT HIFU scan determined the location of the ThermoDots with high spatial-resolution that led to drastic improvement in quantitative accuracy. In this work, all fluorescence images are acquired with a pixel size of 0.25 mm x 0.25 mm, which results from data binning by a factor of 4. Technically, this allowed to increase the fluorescence signal strength during acquisition without degrading our imaging performance. In fact, TMFT is able to improve FMT spatial resolution to ~1.3 mm, which is limited by the size of the hot spot of the HIFU. Therefore, acquiring images with smaller pixel size would not only degrade the quality of the signals, but would be completely meaningless due the HIFU spot size limitation.

Our future work will be adding a structured light scheme to the TMFT system to be able to recover the boundary of the animal, which is necessary for the forward problem resolution step. In addition to that, we will replace the cooled CCD with an intensified CCD camera (ICCD) to amplify the signals and accelerate the total imaging time. Here, an integration time of two seconds is required to acquire each of the FMT images. This slow acquisition time caused by using this CCD camera not only prolonged the total imaging time, but also prevented us from employing our previously developed fast-scan methodology [21]. Nevertheless, the integration time of two seconds used here still allow us to keep the total imaging time to approximately six minutes using the step-and-shoot method described above. We believe that with those improvements CCD-based TMFT will be ready to play an important role in preclinical research.

Funding. National Institutes of Health (P30CA062203, R01EB008716, R21CA170955, R33CA120175); Susan G. Komen (KG101442); Bogazici University (BAP 15362).

Disclosures. The authors declare no conflicts of interest.

Data availability. Data underlying the results presented in this paper are not publicly available at this time but may be obtained from the authors upon reasonable request.

References

1. V. Ntziachristos, "Fluorescence molecular imaging," Annu. Rev. Biomed. Eng. **8**(1), 1–33 (2006).
2. L. V. Wang and H.-I. Wu, *Biomedical Optics: Principles and Imaging* (Wiley, 2007).
3. F. Leblond, S. C. Davis, P. A. Valdes, and B. W. Pogue, "Pre-clinical whole-body fluorescence imaging: Review of instruments, methods and applications," J. Photochem. Photobiol., B **98**(1), 77–94 (2010).
4. S. R. Arridge and J. C. Schotland, "Optical tomography: forward and inverse problems," Inverse Problems **25**(12), 123010 (2009).
5. D. Kepshire, N. Mincu, M. Hutchins, J. Gruber, H. Dehghani, J. Hypnarowski, F. Leblond, M. Khayat, and B. W. Pogue, "A microcomputed tomography guided fluorescence tomography system for small animal molecular imaging," Rev. Sci. Instrum. **80**(4), 043701 (2009).
6. S. C. Davis, B. W. Pogue, R. Springett, C. Leussler, P. Mazurkewitz, S. B. Tuttle, S. L. Gibbs-Strauss, S. S. Jiang, H. Dehghani, and K. D. Paulsen, "Magnetic resonance-coupled fluorescence tomography scanner for molecular imaging of tissue," Rev. Sci. Instrum. **79**(6), 064302 (2008).
7. Y. Lin, W. C. Barber, J. S. Iwanczyk, W. W. Roeck, O. Nalcioglu, and G. Gulsen, "Quantitative fluorescence tomography using a trimodality system: in vivo validation," J. Biomed. Opt. **15**(4), 040503 (2010).
8. J. Gruber, A. Paliwal, H. Ghadyani, E. Maytin, T. Hasan, and B. W. Pogue, "High-frequency ultrasound-guided fluorescence tomography of protoporphyrin IX in subcutaneous tumors," in *Biomedical Optics and 3-D Imaging, OSA Technical Digest (CD)* (Optica Publishing Group, 2010), paper BMB5.
9. A. Ale, R. B. Schulz, A. Sarantopoulos, and V. Ntziachristos, "Imaging performance of a hybrid x-ray computed tomography-fluorescence molecular tomography system using priors," Med. Phys. **37**(5), 1976–1986 (2010).
10. Y. Lin, W. C. Barber, J. S. Iwanczyk, W. Roeck, O. Nalcioglu, and G. Gulsen, "Quantitative fluorescence tomography using a combined tri-modality FT/DOT/XCT system," Opt. Express **18**(8), 7835–7850 (2010).
11. R. X. Xu, J. Huang, J. S. Xu, D. Sun, G. H. Hinkle, E. W. Martin, and S. P. Povoski, "Fabrication of indocyanine green encapsulated biodegradable microbubbles for structural and functional imaging of cancer," J. Biomed. Opt. **14**(3), 034020 (2009).

Biomedical Optics EXPRESS

12. L. Zhou, B. Yazici, and V. Ntziachristos, "Fluorescence molecular-tomography reconstruction with a priori anatomical information," Proc. SPIE 6868, Small Animal Whole-Body Optical Imaging Based on Genetically Engineered Probes, 68680O (13 February 2008).
13. Y. Lin, L. Bolisay, M. Ghijsen, T. C. Kwong, and G. Gulsen, "Temperature-modulated fluorescence tomography in a turbid media," Appl. Phys. Lett. **100**(7), 073702 (2012).
14. B. Yuan, S. Uchiyama, Y. Liu, K. T. Nguyen, and G. Alexandrakis, "High-resolution imaging in a deep turbid medium based on an ultrasound-switchable fluorescence technique," Appl. Phys. Lett. **101**(3), 033703 (2012).
15. S. Yu, T. Yao, and B. Yuan, "An ICCD camera-based time-domain ultrasound-switchable fluorescence imaging system," Sci. Rep. **9**(1), 10552 (2019).
16. R.-L. Liu and R.-Q. Cai, "Recent advances in ultrasound-controlled fluorescence technology for deep tissue optical imaging," J. Pharm. Anal. **12**(4), 530–540 (2022).
17. T. C. Kwong, F. Nouizi, Y. Lin, U. Sampathkumaran, S. Ahmed, and G. Gulsen, "Temperature-modulated fluorescence tomography: modulating tissue temperature using HIFU for high-resolution in vivo fluorescence tomography," in Multimodal Biomedical Imaging VIII *International Society for Optics and Photonics*, 2013, p. 857405.
18. F. Nouizi, T. Kwong, Y. Lin, U. Sampathkumaran, S. Ahmed, and G. Gulsen, "A combined HIFU-fluorescence tomography high-resolution imaging technique using temperature-modulated thermodots," in *Optics in the Life Sciences, OSA Technical Digest (online)* (Optica Publishing Group, 2013), paper JW3B.8.
19. T. C. Kwong, F. Nouizi, Y. Lin, R. Rajyaguru, T. Nguyen, L. Alptekin, U. Sampathkumaran, Y. Zhu, S. Ahmed, and G. Gulsen, "Validation of temperature-modulated fluorescence tomography in vivo," *Multimodal Biomedical Imaging IX, International Society for Optics and Photonics*, 2014, p. 89370 H.
20. Y. Lin, F. Nouizi, T. C. Kwong, and G. Gulsen, "Simulation-based evaluation of the resolution and quantitative accuracy of temperature-modulated fluorescence tomography," Appl. Opt. **54**(25), 7612–7621 (2015).
21. F. Nouizi, T. C. Kwong, J. Cho, Y. Lin, U. Sampathkumaran, and G. Gulsen, "Implementation of a new scanning method for high-resolution fluorescence tomography using thermo-sensitive fluorescent agents," Opt. Lett. **40**(21), 4991–4994 (2015).
22. T. C. Kwong, F. Nouizi, Y. Lin, Y. Zhu, U. Sampathkumaran, and G. Gulsen, "Thermal Outlining using Focused Ultrasound (TOFU) with reversible temperature sensitive fluorescent probes," *Multimodal Biomedical Imaging XI, International Society for Optics and Photonics*, 2016, p. 97010 L.
23. T. C. Kwong, F. Nouizi, Y. Lin, J. Cho, Y. Zhu, U. Sampathkumaran, and G. Gulsen, "Experimental evaluation of the resolution and quantitative accuracy of temperature-modulated fluorescence tomography," Appl. Opt. **56**(3), 521–529 (2017).
24. T. C. Kwong, F. Nouizi, J. Cho, Y. Lin, U. Sampathkumaran, and G. Gulsen, "Feasibility study of high spatial resolution multimodality fluorescence tomography in ex vivo biological tissue," Appl. Opt. **56**(28), 7886–7891 (2017).
25. Y. Chen and X. Li, "Thermo/pH-Responsive and Reversible NIR Fluorescent Probes for Optical Molecular Imaging," in Biomedical Optics and 3-D Imaging, OSA Technical Digest (CD) (Optica Publishing Group, 2010), paper JMA105.
26. T. H. Kim, Y. Chen, C. W. Mount, W. R. Gombotz, X. Li, and S. H. Pun, "Evaluation of temperature-sensitive, indocyanine green-encapsulating micelles for noninvasive near-infrared tumor imaging," Pharm. Res. **27**(9), 1900–1913 (2010).
27. Y. Lin, T. C. Kwong, L. Bolisay, and G. Gulsen, "Temperature-modulated fluorescence tomography based on both concentration and lifetime contrast," J. Biomed. Opt. **17**(5), 056007 (2012).
28. T. C. Kwong, F. Nouizi, U. Sampathkumaran, Y. Zhu, M. M. Alam, and G. Gulsen, "Activatable thermo-sensitive ICG encapsulated pluronic nanocapsules for temperature sensitive fluorescence tomography," Proc. SPIE 9339, *Reporters, Markers, Dyes, Nanoparticles, and Molecular Probes for Biomedical Applications VII*, 93390C (2015).
29. F. Nouizi, T. C. Kwong, J. Ruiz, J. Cho, Y.-W. Chan, K. Ikemura, H. Erkol, U. Sampathkumaran, and G. Gulsen, "A thermo-sensitive fluorescent agent based method for excitation light leakage rejection for fluorescence molecular tomography," Phys. Med. Biol. **64**(3), 035007 (2019).
30. F. Nouizi, T. C. Kwong, J. Kwong, J. Cho, Y. Chan, U. Sampathkumaran, Y. Zhu, M. M. Alam, and G. Gulsen, "Excitation light leakage suppression using temperature sensitive fluorescent agents," *Proc. SPIE 9319, Optical Tomography and Spectroscopy of Tissue XI, 93190Y* (12 March 2015).
31. F. Nouizi, M. Torregrossa, O. Geneveaux, R. Chabrier, and P. Poulet, "3D modeling of noncontact fiber-based approach for time-resolved diffuse optical tomography," *Proc. SPIE 7896, Optical Tomography and Spectroscopy of Tissue IX, 78961Z* (17 February 2011).
32. F. Nouizi, R. Chabrier, M. Torregrossa, and P. Poulet, "3D modeling for solving forward model of no-contact fluorescence diffuse optical tomography method," Proc. SPIE 7369, *Diffuse Optical Imaging II*, 73690C (2009).
33. M. Mehrabi, F. Nouizi, M. Algarawi, T. C. Kwong, H. Erkol, U. Sampathkumaran, and G. Gulsen, "CCD-based temperature modulated fluorescence tomography," Proc. SPIE 10874, *Optical Tomography and Spectroscopy of Tissue XIII*, 108740Y (2019).
34. D. Nikkhah, F. Nouizi, R. Hurtado, P. Tabatabaei, and G. Gulsen, "Temperature Modulated Fluorescence Tomography Feasibility Using an Intensified CCD Camera," in *Biophotonics Congress: Biomedical Optics 2022 (Translational, Microscopy, OCT, OTS, BRAIN), Technical Digest Series* (Optica Publishing Group, 2022), paper JM3A.9.
35. T. C. Kwong, "A new modality for high resolution diffuse optical imaging: Temperature modulated fluorescence tomography," UC Irvine (2017).

Biomedical Optics EXPRESS

36. Y. Lin, H. Yan, O. Nalcioglu, and G. Gulsen, "Quantitative fluorescence tomography with functional and structural a priori information," Appl. Opt. **48**(7), 1328–1336 (2009).
37. S. R. Arridge, "Optical tomography in medical imaging," Inverse Problems **15**(2), R41–R93 (1999).
38. F. Nouizi, H. Erkol, A. Luk, M. Marks, M. B. Unlu, and G. Gulsen, "An accelerated photo-magnetic imaging reconstruction algorithm based on an analytical forward solution and a fast Jacobian assembly method," Phys. Med. Biol. **61**(20), 7448–7465 (2016).
39. F. Nouizi, A. Luk, D. Thayer, Y. Lin, S. Ha, and G. Gulsen, "Experimental validation of a high-resolution diffuse optical imaging modality: photomagnetic imaging," J. Biomed. Opt. **21**(1), 016009 (2016).
40. F. Nouizi, H. Erkol, A. Luk, M. B. Unlu, and G. Gulsen, "Real-time photo-magnetic imaging," Biomed. Opt. Express **7**(10), 3899–3904 (2016).
41. H. Erkol, F. Nouizi, M. B. Unlu, and G. Gulsen, "An extended analytical approach for diffuse optical imaging," Phys. Med. Biol. **60**(13), 5103–5121 (2015).
42. F. Nouizi, M. Torregrossa, R. Chabrier, and P. Poulet, "Improvement of absorption and scattering discrimination by selection of sensitive points on temporal profile in diffuse optical tomography," Opt. Express **19**(13), 12843–12854 (2011).
43. K. Levenberg, "A method for the solution of certain non–linear problems in least squares," Q. Appl. Math. **2**(2), 164–168 (1944).
44. D. W. Marquardt, "An algorithm for least-squares estimation of nonlinear parameters," J. Soc. Indust. Appl. Math. **11**(2), 431–441 (1963).
45. F. Nouizi, H. Erkol, A. Luk, Y. Lin, and G. Gulsen, "Analytical Photo Magnetic Imaging," in *Biomedical Optics 2016, OSA Technical Digest (online)* (Optica Publishing Group, 2016), paper OW4D.7.
46. P. K. Yalavarthy, B. W. Pogue, H. Dehghani, C. M. Carpenter, S. Jiang, and K. D. Paulsen, "Structural information within regularization matrices improves near infrared diffuse optical tomography," Opt. Express **15**(13), 8043–8058 (2007).
47. W. Wan, Y. Wang, J. Qi, L. Liu, W. Ma, J. Li, L. Zhang, Z. Zhou, H. Zhao, and F. Gao, "Region-based diffuse optical tomography with registered atlas: in vivo acquisition of mouse optical properties," Biomed. Opt. Express **7**(12), 5066–5080 (2016).
48. Y. Lin, H. Gao, O. Nalcioglu, and G. Gulsen, "Fluorescence diffuse optical tomography with functional and anatomical a priori information: feasibility study," Phys. Med. Biol. **52**(18), 5569–5585 (2007).
49. F. Nouizi, R. Chabrier, M. Torregrossa, and P. Poulet, "Time-Resolved Optical Tomography in Preclinical Studies: Propagation of Excitation and Fluorescence Photons," *Comsol Conference, Hannover, Germany*, 2008.